Published in final edited form as:
J Magn Reson. 2012 April ; 217: 92–99. doi:10.1016/j.jmr.2012.02.020.

Dual-band selective double cross polarization for heteronuclear polarization transfer between dilute spins in solid-state MAS NMR

Zhengfeng Zhang[a], **Yimin Miao**[b,c], **Xiaoli Liu**[a], **Jun Yang**[a,*], **Conggang Li**[a], **Feng Deng**[a], and **Riqiang Fu**[c,*]

[a]Wuhan Center for Magnetic Resonance, State Key Laboratory of Magnetic Resonance and Atomic and Molecular Physics, Wuhan Institute of Physics and Mathematics, Chinese Academy of Science, Wuhan 430071, PR China

[b]Department of Chemistry and Biochemistry, Florida State University, Tallahassee, FL 32306, USA

[c]National High Magnet Field Lab, Tallahassee, FL 32310, USA

Abstract

A sinusoidal modulation scheme is described for selective heteronuclear polarization transfer between two dilute spins in double cross polarization magic-angle-spinning nuclear magnetic resonance spectroscopy. During the second N → C cross polarization, the ^{13}C RF amplitude is modulated sinusoidally while the ^{15}N RF amplitude is tangent. This modulation induces an effective spin-lock field in two selective frequency bands in either side of the ^{13}C RF carrier frequency, allowing for simultaneous polarization transfers from ^{15}N to ^{13}C in those two selective frequency bands. It is shown by experiments and simulations that this sinusoidal modulation allows one to selectively polarize from ^{15}N to its covalently bonded ^{13}Cα and ^{13}C′ carbons in neighboring peptide planes simultaneously, which is useful for establishing the back-bone connectivity between two sequential residues in protein structural elucidation. The selectivity and efficiency were experimentally demonstrated on a uniformly ^{13}C,^{15}N-labeled β1 immunoglobulin binding domain of protein G (GB1).

Keywords

Double cross polarization (DCP); NCA/NCO; Solid-state MAS NMR; Heteronuclear polarization transfer

1. Introduction

In the past decade, solid-state magic-angle-spinning (MAS) NMR has rapidly emerged as a powerful technique for studying insoluble proteins such as membrane proteins, amyloid proteins, and supramolecules. Resonance assignment is an essential step in the structural determination of uniformly ^{15}N and ^{13}C labeled proteins. In this regard, sequential assignments have been commonly used to extract structural constraints [1–12] via through-spaced dipolar couplings in well designed multi-dimensional experiments based on heteronuclear [13,14] and homonuclear dipolar recoupling [15–25] techniques in solid-state

*Corresponding authors. Address: 1800 E. Paul Dirac Drive, Tallahassee, FL 32310, USA. Fax: +1 850 644 1366 (R. Fu). yangjun@wipm.ac.cn (J. Yang), rfu@magnet.fsu.edu (R. Fu).

MAS NMR. While the heteronuclear correlation between ^{13}C and ^{15}N is one of the most important experiments in such sequential assignments, due to the fact that each backbone nitrogen covalently bonds with the Cα and carbonyl (C′) carbons in neighboring peptide planes, thus providing useful through-bond links between two sequential residues.

The heteronuclear polarization transfer between ^{13}C and ^{15}N can be achieved by the so-called double cross polarization, i.e. DCP [13,26,27], in which ^{15}N is first polarized from the abundant ^{1}H spins and then transferred to ^{13}C via a second cross polarization from ^{15}N to ^{13}C. Whereas the ^{1}H–^{15}N or ^{1}H–^{13}C CP are relatively mature, most of the issues regarding DCP are primarily focused on the second N → C CP involving polarization transfer, in terms of selectivity, efficiency, and the influence of RF instability, between two low-γ nuclear species [28–42]. For example, SPECIFIC CP [31], a DCP experiment with carefully adjusted offsets and RF amplitudes on both the ^{13}C and ^{15}N channels, leads to selective polarization transfer from ^{15}N to one of its bonded ^{13}Cs (either $^{13}C\alpha$ or $^{13}C'$), known as the two-dimensional (2D) NCA and NCO experiments, respectively. With the two NCA and NCO spectra, the connectivity between the Cα[i] and C′ [i–1] in the adjacent peptide planes can thus be established through N[i]. Alternatively, in the CANCO experiments [43], the $^{13}C\alpha$[i] is first selectively polarized from ^{1}H, and then sequentially transferred to $^{13}C'$ [i–1] through two-step selective polarization transfers (i.e. from $^{13}C\alpha$ [i] → ^{15}N[i] and then from ^{15}N[i] → $^{13}C'$[i–1]). However, such three-dimensional (3D) experiments (if including the ^{15}N chemical shift dimension) suffer from very low sensitivity due to the multistep polarization transfers among the dilute spins. The efficiency for each heteronuclear polarization transfer between ^{13}C and ^{15}N is around 30–40%. Therefore, there is only 10–15% polarization transfer efficiency from $^{13}C\alpha$[i] to $^{13}C'$[i–1] [43].

In this work, we propose a dual-band selective double cross polarization to simultaneously polarize the $^{13}C\alpha$[i] and $^{13}C'$[i–1] from ^{15}N[i], which allows one to establish the backbone $^{13}C\alpha$[i]–^{15}N[i]–$^{13}C'$[i–1] connectivity in a single 2D ^{15}N–^{13}C correlation spectrum, rather than in the two NCA and NCO spectra or in a low-sensitive CANCO spectrum, provided that there is a sufficient resolution in the ^{15}N dimension. In this new scheme, the RF amplitude of the ^{13}C channel is modulated sinusoidally while that of the ^{15}N channel is kept constant or tangent-modulated during the second N → C CP. This sinusoidal modulation [44,45] directly applies the RF amplitude onto the Cα and C′ chemical shift regions simultaneously, even if the carrier frequency is away from those regions. The modulation period needs not to be commensurate with the period of sample rotation. We refer to this new method as sine-modulated double cross polarization (smDCP). It will be shown by experiments and simulations that smDCP can be effectively used for the dual-band selective heteronuclear polarization transfer using low RF amplitudes, thus improving selectivity and relaxing the demand on ^{1}H decoupling power. The advantages of this new scheme will be illustrated by using a uniformly ^{13}C,^{15}Nlabeled β1 immunoglobulin binding domain of protein G (GB1) in the following sections.

2. Materials and experiments

The 56-residue β1 immunoglobulin binding domain of protein G (GB1) was expressed in E. coli BL21 (DE3) and minimal media (1.0 g/L ^{15}N NH4Cl, 2.0 g/L ^{13}C glucose), induced with 1.0 mM isopropyl β-D-thiogalactoside (IPTG) for 4 h. The cell pellet was resuspended in PBS buffer (50 mM Phosphate, 150 mM NaCl, pH 8.0) and incubated at 80 °C for 5 min. After centrifugation at 10,000 rpm for 30 min, the supernatant was purified by ion exchange (AKTA purifier 10.0), gelfiltration (Sephadex 100) and following desalination (AKTA purifier 10.0) with phosphate buffer (pH 8.0). The precipitation of GB1 was incubated over night at 4 °C in precipitation solution of 33% isopropanol (IPA) and 67% 2-

methylpentane-2,4-diol (MPD). The final microcrystals were centrifuged at 5000 rpm for 2 min and transferred into a 4 mm rotor.

All the NMR experiments were performed on a wide-bore Varian 600 MHz NMR spectrometer of VNMRS system, equipped with a 4 mm triple-resonance T3-HXY MAS probe, at a temperature of 283 K (calibrated in separate experiments using the lead nitrate sample [46]). The sample spinning rate was set to 11 kHz ± 2 Hz. Fig. 1 shows the pulse sequences used in our experiments. The ^{1}H $\pi/2$ pulse was 3.3 μs, while the ^{13}C π pulse length of 7.2 μs was used for decoupling in the ^{15}N chemical shift dimension (i.e., t_1 dimension). During the first ^{1}H–^{15}N CP with a contact time of 1.2 ms, the ^{15}N RF amplitude was about 37 kHz and the ^{1}H RF-field was ramped from 90% to 110% of 57 kHz. The contact time for the second N → C CP was set to 5 ms, while the ^{15}N and ^{13}C RF amplitudes were varied depending upon the experimental schemes and will be described in their corresponding figures. The SPINAL-64 [47] sequence with 71 kHz RF amplitude and a 7.9 μs flip pulse was applied during both t_1 and t_2 dimension for ^{1}H decoupling, while an 83 kHz CW decoupling was used during the ^{15}N–^{13}C contact. The ^{13}C chemical shifts were referenced to adamantane at 40.48 ppm of the downfield signal [48] and the ^{15}N reference was calculated based on the gyromagnetic ratio as recommended by IUPAC [49]. The RF amplitudes were calculated based on several measured amplitudes with the GB1 sample and the linearity of Varian linear amplifiers.

Fig. 1(I) shows the standard N → C CP scheme where the ^{15}N RF amplitude is tangent while the ^{13}C RF amplitude remains constant, or vice versa, to enhance the CP efficiency [30,50]. For comparison, we use the rectangular ^{13}C RF amplitude in our standard DCP experiments and refer it as ‘rectangular DCP’ in the following discussions. While in the smDCP scheme, the ^{15}N RF amplitude is tangent while the ^{13}C RF amplitude ω_{1C} is sinusoidally modulated, as shown in Fig. 1(II):

$$\omega_{1C}(t)=\omega_{1C}^{max}\sin(\omega_m t), \quad (1)$$

where, ω_{1C}^{max} and ω_m represent the maximum RF amplitude and the modulation frequency, respectively. Mathematically, such a sine-wave modulation induces a spin-lock field in two frequency bands positioning at distances of $\pm\omega_m$ away from the carrier frequency, which allows for polarization transfers from ^{15}N to ^{13}C in these two frequency bands. While the effective RF amplitude applied on these two frequency bands is just about half of the maximum RF amplitude ω_{1C}^{max}.

3. Results and discussion

Fig. 2 shows the one-dimensional (1D) ^{13}C spectra of the GB1 sample spinning at 11 kHz recorded under different N → C polarization conditions. With the direct CP from ^{1}H to ^{13}C, all ^{13}C resonances were observed, as shown in Fig. 2A. Fig. 2B and C show the SPECIFIC CP spectra using the rectangular DCP scheme (e.g. Fig. 1I) with the selective polarization pathway from ^{15}N to ^{13}Cα and ^{13}C′, respectively. In these experiments, the ^{13}C carrier frequency was set closely to either Cα or C′ region and its RF amplitude was chosen to be low in order to achieve the required selectivity. The efficiency for these SPECIFIC CP experiments was ~50% as compared to the direct CP from ^{1}H to ^{13}C. If the ^{13}C carrier frequency was set to the mid way between the Cα and C′ regions, the rectangular DCP experiment could also select both the ^{13}Cα and ^{13}C′ region simultaneously with a carefully adjusted RF amplitude [13,30,51], as shown in Fig. 2D. However, both simulations (not shown) and experiments indicate that higher ^{13}C RF amplitude is needed for such a dual-band selectivity. Unfortunately, using the higher RF amplitude compromises the selectivity. As can be seen in Fig. 2D, small aliphatic carbon resonances (from 15 to 40 ppm), as well as

the spinning sidebands at around 100 ppm, appear to be visible. Moreover, for the glycine $^{13}C\alpha$ region (~42 ppm), the signal intensities seem to be much smaller than that in the SPECIFIC CP spectrum. The efficiency for this dual-band selectivity was ~34%, as compared to the spectrum in Fig. 2A.

On the other hand, for the sine modulation scheme, even if the ^{13}C carrier is set far away from the targeted region, the modulation effectively compensates the carrier offset, such that low RF amplitude can be used to achieve the needed selectivity. As shown in Fig. 2E and F, the ^{13}C carrier frequency was set to ±16.667 kHz away from the Cα and C′ regions, respectively. With the sine modulation frequency of 16.667 kHz and a low ^{13}C RF amplitude of 6.0 kHz, the Cα and C′ resonances were selectively polarized. As shown in the figures, the smDCP spectra are almost identical to their respective SPECIFIC CP spectra, with an efficiency of ~50% as compared to the spectrum in Fig. 2A. This implies that both frequency bands induced by the sine modulation in either side of the carrier frequency can be used for the efficient N → C polarization transfer. When the ^{13}C carrier was set to the mid way between the Cα and C′ regions and the modulation frequency matched 8.889 kHz (half of the distance between the Cα and C′ regions), both the $^{13}C\alpha$ and $^{13}C'$ regions were selected simultaneously with the efficiency of 37%, as shown in Fig. 2G. Apparently, the selectivity was comparable with that in the SPECIFIC NCO and NCA experiments, while the unwanted signals appearing in Fig. 2D was *not* observed in the spectrum, owing to the use of the low ^{13}C RF amplitude.

Fig. 3 shows the 2D ^{15}N–^{13}C heteronuclear correlation spectra of the uniformly ^{13}C,^{15}N-labeled GB1 under different polarization conditions. Fig. 3A shows the SPECIFIC NCO (left) and NCA (right) spectra recorded in the separate experiments where the ^{13}C carrier frequency was set closely to the C′ and Cα regions, respectively. Since our sample was prepared at pH 8.0, different from pH 5.5 used in the GB1 sample preparation in the literature [52], the protein's nano-crystalline form might be different. Thus, it is not surprising that the GB1 samples at different pHs gave rise to slightly different resonance patterns in the NCO and NCA spectra. However, their spectral resolution in both ^{13}C and ^{15}N dimensions are comparable [52], confirming that our sample was well prepared. It is worth noting that the slight difference in the resonance patterns resulting from the sample preparations should not affect any conclusion derived in this paper. Fig. 3A shows some partial assignments. Fortunately many resonances could be recognized based on the GB1 assignments as reported in the literature[53], despite the fact that there exist some additional peaks, such as the ones near the T49N-Cα and T49N-A48CO resonances. Fig. 3B shows the dual-band ^{15}N–$^{13}C'$/$^{13}C\alpha$ rectangular DCP spectrum using the rectangular ^{13}C RF field during the N → C contact. Overall, the ^{15}N–^{13}C resonance patterns are similar to their respective SPECIFIC NCO and NCA spectra in Fig. 3A. However, some resonances such as the Gly ^{15}N–$^{13}C\alpha$ resonances (G9N–Cα, G14N–Cα, G38N–Cα, and G41N–Cα) become very weak, while other resonances that did not appear in the SPECIFIC CP spectra started to show up in the spectrum (such as the peak in the left side of the T25N–Cα resonance), implying that the selectivity over the dual bandwidths is hardly uniform, which was also seen in 1D spectrum (e.g. Fig. 2D). It is worth noting that additional cross-peaks around (115 ppm, 103 ppm) and (141 ppm, 41 ppm) (not shown in the spectrum) should belong to the sidebands of $^{13}C'$ and ^{15}N and to the folded-in aliphatic ^{13}C and ^{15}N in sidechains. Thus, the selectivity for the dual-band rectangular DCP is poor owing to the use of the required large ^{13}C RF amplitude during the N → C contact.

Fig. 3C shows the single-band ^{15}N–$^{13}C'$ (left) and ^{15}N–$^{13}C\alpha$ (right) smDCP spectra using the sine modulated ^{13}C RF amplitude during the N → C contact. It can be clearly noted that these spectra are almost identical to those in Fig. 3A, except for the one appearing at (112 ppm and 179 ppm) (below the T11 N-K10CO resonance), again implying that the frequency

bandwidths induced by the sine modulation in both sides of the carrier frequency can be used for selective N → C polarization transfer. Fig. 3D shows the dual-band selective ^{15}N–^{13}C′/^{13}Cα smDCP spectrum when the two frequency bandwidths induced by the sine modulation fell into the C′ and Cα regions simultaneously. Clearly, the resonance patterns in both the ^{15}N–^{13}C′ and ^{15}N–^{13}Cα regions are almost the same as in the single-band selective ^{15}N–^{13}C′and ^{15}N–^{13}Cα spectra as shown in Fig. 3A and C, despite the fact that a few additional peaks, such as (130 ppm and 180 ppm), (130 ppm and 61 ppm) and (118 ppm and 68 ppm), start to appear or gain in intensity. However, the Gly resonances, which almost disappeared in Fig. 3B, were as intensive as in the single-band selective ^{15}N–^{13}C′ and ^{15}N–^{13}Cα spectra as shown in Fig. 3A and C. On the other hand, those unwanted resonances appearing at around (115 ppm, 103 ppm) and (141 ppm, 41 ppm) in Fig. 3B completely disappeared in the dual-band selective ^{15}N–^{13}C′/^{13}Cα smDCP spectrum. Thus, it is concluded that this sine modulation scheme provides an excellent selectivity.

Fig. 4 shows the three 1D slices taken along T49N (Top), N37N (Middle), and V29N (Bottom) from the 2D SPECIFIC NCO/NCA spectra in Fig. 3A and from the smDCP NC spectrum in Fig. 3D, respectively. From their relative intensities, it can be noticed that the signal-to-noise (S/N) ratio for the dual-band selective smDCP is about 68–74% of that for the SPECIFIC NCO/NCA, which is consistent with the observation of the efficiency in the 1D spectra (c.f. Fig. 2). Therefore, the S/N for a single dual-banded smDCP spectrum (in the same overall time by doubling the number of scans) should be comparable to the two separate SPECIFIC NCO/NCA spectra. Our experimental result is beyond what is expected from the fact that the S/N for the dual-banded smDCP is considered to be half of that for SPECIFIC CP since the ^{15}N magnetization is transferred to both carbon sites in the former scheme as compared to only one site in the latter scheme. However, one has to realize that such an expectation holds only when the ^{15}N magnetization is completely transferred to the ^{13}C and/or there exhibits the same spin dynamics during the N → C CP. Due to the fact that the C–N dipolar coupling is very small (~ a few kHz), the polarization transfer rate from N to C is rather slow. A few millisecond CP contact time (e.g. 5 ms in our experiments) can hardly transfer the ^{15}N magnetization completely to ^{13}C. On the other hand, the spin dynamics during the N → C CP may be different in these two schemes since they exhibit different spin systems during CP (N–C for SPECIFIC CP and C–N–C for the dual-banded smDCP). Such a difference might lead to different spin dynamics, as been observed in different ^{1}H–S systems [56–58].

In the DCP experiments, low ^{13}C RF amplitude in the N → C polarization transfer will relax the demand on the ^{1}H decoupling field during the N → C contact. In our experiments, the maximum ^{13}C RF amplitude ω_{1C}^{max} used in the dual-band selective smDCP experiments (e.g. Fig. 2G) was about one-third of that used in the dual-band rectangular DCP experiments (e.g. Fig. 2D). Fig. 5 shows the dependence of the N → C polarization efficiency as a function of the applied ^{1}H decoupling power during the N → C contact. As the ^{1}H decoupling power decreasing from 85 to about 71 kHz, the polarization efficiency from N → Cα dropped to about 60% and 80% for the rectangular and sine modulated DCP schemes, respectively, while the efficiency from N → C′ decreased to ~75% and 90% in their respective spectra. It appears that the ^{1}H decoupling power is more influential on the Cα carbons, probably owing to the strength of dipolar interactions between ^{1}H and ^{13}C as well as the difference between the applied ^{1}H decoupling and the ^{13}C RF amplitude during the N → C contact. A large difference between the ^{1}H decoupling and ^{13}C RF amplitude during the N → C contact is needed to provide sufficient mismatch between the ^{1}H and ^{13}C spins to avoid potential spin exchange between the two spins, especially when they possess a stronger dipolar coupling. Therefore, this might be the reason why the ^{15}N → ^{13}Cα polarization efficiency for the Gly residues was much worse in the dual-band rectangular

DCP (e.g. Fig. 3B) than in the dual-band smDCP experiments (e.g. Fig. 3D). Indeed, the former experiment required five times higher ^{13}C RF amplitude than the latter one under the same ^{1}H decoupling power of 83 kHz during the N → C contact.

It had been reported that the parameters in the DCP experiments were sensitive to experimental settings, such as MAS speed, frequency offset and RF fields [33,38,39]. The influence of instability of ^{13}C RF-field on the N → C polarization efficiency is also investigated for the dual-band polarization transfers, as shown in Fig. 6. It can be seen in Fig. 6A that the ^{15}N → ^{13}Cα and ^{15}N → ^{13}C′ polarization efficiencies for the rectangular DCP scheme suffer severely from the variation of ^{13}C RF amplitude and decrease to about 30– 50% with about 10% variation. On the other hand, for the smDCP scheme the efficiency from ^{15}N → ^{13}Cα was just slightly affected by the ^{13}C RF variation, while about 70% efficiency from ^{15}N → ^{13}C′ was preserved. Thus, there is an advantage to use this sine modulation scheme in long duration experiments.

Fig. 7 shows the simulated selectivity for the sine modulation scheme (e.g. Fig. 1II) as a function of offset and modulation frequency ω_m. In the simulations, the experimental parameters of ω_{1N} = 9 kHz, ω_{1C}^{max}=6 kHz, and the MAS rate of 11 kHz were used. Clearly, the frequency selective bandwidth (i.e. the offset range within which the polarization efficiency is above 60%) was about ω_m ± 2 kHz, apparently independent of the spinning rate. In other words, the selective bandwidth is about ±2 kHz at distances of ±ω_m away from the carrier frequency. This bandwidth is independent of spinning rate but depends on the RF amplitude ω_{1C}^{max} used in the experiments. For a better selectivity, low-power RF amplitude is always preferable. Our simulations (not shown here) suggest that the dual-banded smDCP scheme should be effective at the magnetic field B_0 up to 18.8 T with the spinning rate of 25 kHz. However, at very high fields where the chemical shift anisotropy (CSA) interactions become significant, there is a potential that the efficiency and selectivity could be compromised when using low-power RF amplitude which becomes unable to spin-lock the magnetization during the N → C CP. It has been demonstrated recently [60] that low-power symmetry-based band-selective sequences appear to be an effective approach for applications in high fields and fast sample spinning.

4. Conclusion

We have demonstrated that sinusoidal modulation of the ^{13}C RF amplitude during the second N → C cross polarization in double cross polarization (DCP) MAS NMR spectroscopy provides an effective spin-lock field in two selective frequency bands in either side of the ^{13}C RF carrier frequency, allowing for simultaneous polarization transfers from ^{15}N to ^{13}C in those two selective frequency bands. When the two frequency bands fall into the C′ and Cα regions, the dual-band selective heteronuclear polarization transfer from ^{15}N to both ^{13}C′ and ^{13}Cα can be achieved simultaneously in one experiment, rather than in two separate SPECIFIC NCO and NCA experiments or in a low-sensitive CANCO experiment, which is useful for establishing the backbone connectivity between two sequential residues in protein structural elucidation. It should be recognized that this information about the sequential Cα[i]–N[i]–C′[i–1] topology alone is not sufficient to obtain sequential resonance assignments. It has to be combined with other 2D or 3D experiments such as NCACX/NCOCX and/or ^{13}C–^{13}C correlation experiments. With the ability of selecting both the backbone Cα and C′ carbons, some elaborate 2D or 3D experiments could be designed to simplify crowded resonances typically observed in ^{13}C–^{13}C correlation spectra of biological samples being studied and to help assigning resonances, especially when combined with specific labeling approaches such as glycerol labeling strategy. For the dual-band selective polarization transfer, this new scheme greatly relaxes the demand on both ^{13}C and ^{1}H decoupling amplitudes. As compared to standard

DCP experiments, this sine modulated scheme is also less sensitive to the instability of the ^{13}C RF field. Moreover, such a modulation could also be applicable for dual-band selective heteronuclear polarization transfer between other spin pairs, as mentioned by Baldus et al. [31], such as ^{19}F, ^{31}P and even ^{1}H in paramagnetic systems, with the use of a moderate RF amplitude when applied to the spin that has a large chemical shift distribution, especially under fast MAS condition [45].

Acknowledgments

This work was supported in part by the CAS/SAFEA International Partnership Program for Creative Research Teams and by Grants from the National Natural Science Foundation of China (21075133, 21173259, 20921004) and the National Basic Research Program of China (2009CB918600). Y.M. and R.F. are grateful for support from the National Institute of Health (NIH) Grant AI23007.

References

1. Takegoshi K, Nakamura S, Terao T. C-13–H-1 dipolar-assisted rotational resonance in magic-angle spinning NMR. Chem Phys Lett. 2001; 344:631–637.
2. Castellani F, van Rossum B, Diehl A, Schubert M, Rehbein K, Oschkinat H. Structure of a protein determined by solid-state magic-angle-spinning NMR spectroscopy. Nature. 2002; 420:98–102. [PubMed: 12422222]
3. Jaroniec CP, Filip C, Griffin RG. 3D TEDOR NMR experiments for the simultaneous measurement of multiple carbon–nitrogen distances in uniformly C-13, N-15-labeled solids. J Am Chem Soc. 2002; 124:10728–10742. [PubMed: 12207528]
4. Morcombe CR, Gaponenko V, Byrd RA, Zilm KW. Diluting abundant spins by isotope edited radio frequency field assisted diffusion. J Am Chem Soc. 2004; 126:7196–7197. [PubMed: 15186155]
5. Lewandowski JR, De Paepe G, Griffin RG. Proton assisted insensitive nuclei cross polarization. J Am Chem Soc. 2007; 129:728–729. [PubMed: 17243786]
6. De Paepe G, Lewandowski JR, Loquet A, Bockmann A, Griffin RG. Proton assisted recoupling and protein structure determination. J Chem Phys. 2008; 129
7. Scholz I, Huber M, Manolikas T, Meier BH, Ernst M. MIRROR recoupling and its application to spin diffusion under fast magic-angle spinning. Chem Phys Lett. 2008; 460:278–283.
8. Weingarth M, Demco DE, Bodenhausen G, Tekely P. Improved magnetization transfer in solid-state NMR with fast magic angle spinning. Chem Phys Lett. 2009; 469:342–348.
9. Scholz I, Meier BH, Ernst M. NMR polarization transfer by second-order resonant recoupling: RESORT. Chem Phys Lett. 2010; 485:335–342.
10. Weingarth M, Bodenhausen G, Tekely P. Broadband magnetization transfer using moderate radio-frequency fields for NMR with very high static fields and spinning speeds. Chem Phys Lett. 2010; 488:10–16.
11. Hou GJ, Yan S, Sun SJ, Han Y, Byeon IJL, Ahn J, Concel J, Samoson A, Gronenborn AM, Polenova T. Spin diffusion driven by R-symmetry sequences: applications to homonuclear correlation spectroscopy in MAS NMR of biological and organic solids. J Am Chem Soc. 2011; 133:3943–3953. [PubMed: 21361320]
12. Hu BW, Lafon O, Trebosc J, Chen Q, Amoureux JP. Broad-band homonuclear correlations assisted by (1)H irradiation for bio-molecules in very high magnetic field at fast and ultra-fast MAS frequencies. J Magn Reson. 2011; 212:320–329. [PubMed: 21873091]
13. Schaefer J, McKay RA, Stejskal EO. Double-cross-polarization NMR of solids. J Magn Reson. 1979; 34:443–447.
14. Hing AW, Vega S, Schaefer J. Transferred-echo double-resonance NMR. J Magn Reson. 1992; 96:205–209.
15. Raleigh DP, Levitt MH, Griffin RG. Rotational resonance in solid-state NMR. Chem Phys Lett. 1988; 146:71–76.
16. Tycko R, Dabbagh G. Measurement of nuclear magnetic dipole–dipole couplings in magic angle spinning NMR. Chem Phys Lett. 1990; 173:461–465.

17. Bennett AE, Ok JH, Griffin RG, Vega S. Chemical shift correlation spectroscopy in rotating solids: radio frequency-driven dipolar recoupling and longitudinal exchange. J Chem Phys. 1992; 96:8624–8627.
18. Tycko R, Smith SO. Symmetry principles in the design of pulse sequences for structural measurements in magic angle spinning nuclear-magnetic-resonance. J Chem Phys. 1993; 98:932–943.
19. Nielsen NC, Bildsoe H, Jakobsen HJ, Levitt MH. Double-quantum homonuclear rotary resonance: efficient dipolar recovery in magic-angle- spinning nuclear-magnetic-resonance. J Chem Phys. 1994; 101:1805–1812.
20. Gregory DM, Mitchell DJ, Stringer JA, Kiihne S, Shiels JC, Callahan J, Mehta MA, Drobny GP. Windowless dipolar recoupling: the detection of weak dipolar couplings between spin-1/2 nuclei with large chemical-shift anisotropies. Chem Phys Lett. 1995; 246:654–663.
21. Lee YK, Kurur ND, Helmle M, Johannessen OG, Nielsen NC, Levitt MH. Efficient dipolar recoupling in the NMR of rotating solids: a sevenfold symmetrical radiofrequency pulse sequence. Chem Phys Lett. 1995; 242:304–309.
22. Sun BQ, Costa PR, Kocisko D, Lansbury PT, Griffin RG. Internuclear distance measurements in solid state nuclear magnetic resonance: dipolar recoupling via rotor synchronized spin locking. J Chem Phys. 1995; 102:702–707.
23. Hohwy M, Jakobsen HJ, Eden M, Levitt MH, Nielsen NC. Broadband dipolar recoupling in the nuclear magnetic resonance of rotating solids: a compensated C7 pulse sequence. J Chem Phys. 1998; 108:2686–2694.
24. Verel R, Baldus M, Ernst M, Meier BH. A homonuclear spin-pair filter for solid-state NMR based on adiabatic-passage techniques. Chem Phys Lett. 1998; 287:421–428.
25. Hohwy M, Rienstra CM, Jaroniec CP, Griffin RG. Fivefold symmetric homonuclear dipolar recoupling in rotating solids: application to double quantum spectroscopy. J Chem Phys. 1999; 110:7983–7992.
26. Schaefer J, Stejskal EO, Garbow JR, McKay RA. Quantitative determination of the concentrations of C-13–N-15 chemical bonds by double cross-polarization NMR. J Magn Reson. 1984; 59:150–156.
27. Stejskal EO, Schaefer J, McKay RA. Analysis of double cross-polarization rates in solid proteins. J Magn Reson. 1984; 57:471–485.
28. Wu XL, Zilm KW. Cross-polarization with high-speed magic-angle-spinning. J Magn Reson, Ser A. 1993; 104:154–165.
29. Sun BQ, Costa PR, Griffin RG. Heteronuclear polarization transfer by radiofrequency-driven dipolar recoupling under magic-angle-spinning. J Magn Reson, Ser A. 1995; 112:191–198.
30. Baldus M, Geurts DG, Hediger S, Meier BH. Efficient N-15–C-13 polarization transfer by adiabatic-passage Hartmann–Hahn cross polarization. J Magn Reson, Ser A. 1996; 118:140–144.
31. Baldus M, Petkova AT, Herzfeld J, Griffin RG. Cross polarization in the tilted frame: assignment and spectral simplification in heteronuclear spin systems. Mol Phys. 1998; 95:1197–1207.
32. Brinkmann A, Levitt MH. Symmetry principles in the nuclear magnetic resonance of spinning solids: heteronuclear recoupling by generalized Hartmann–Hahn sequences. J Chem Phys. 2001; 115:357–384.
33. Bjerring M, Nielsen NC. Solid-state NMR heteronuclear coherence transfer using phase and amplitude modulated rf irradiation at the Hartmann–Hahn sideband conditions. Chem Phys Lett. 2003; 382:671–678.
34. Kehlet CT, Sivertsen AC, Bjerring M, Reiss TO, Khaneja N, Glaser SJ, Nielsen NC. Improving solid-state NMR dipolar recoupling by optimal control. J Am Chem Soc. 2004; 126:10202–10203. [PubMed: 15315406]
35. Khaneja N. Sensitivity enhanced recoupling experiments in solid-state NMR by gamma preparation. J Magn Reson. 2006; 183:242–251. [PubMed: 16997586]
36. Khaneja N, Kehlet C, Glaser SJ, Nielsen NC. Composite dipolar recoupling: anisotropy compensated coherence transfer in solid-state nuclear magnetic resonance. J Chem Phys. 2006; 124:114503. [PubMed: 16555897]

37. Kehlet C, Bjerring M, Sivertsen AC, Kristensen T, Enghild JJ, Glaser SJ, Khaneja N, Nielsen NC. Optimal control based NCO and NCA experiments for spectral assignment in biological solid-state NMR spectroscopy. J Magn Reson. 2007; 188:216–230. [PubMed: 17681479]
38. Yang JH, Chou FC, Tzou DLM. Coherence selection in double CP MAS NMR spectroscopy. J Magn Reson. 2008; 195:116–120. [PubMed: 18782675]
39. Lin J, Bayro MJ, Griffin RG, Khaneja N. Dipolar recoupling in solid state NMR by phase alternating pulse sequences. J Magn Reson. 2009; 197:145–152. [PubMed: 19157931]
40. Bjerring M, Nielsen AB, Tosner Z, Nielsen NC. Broadband heteronuclear dipolar recoupling without (1)H decoupling in solid-state NMR using simple cross-polarization methods. Chem Phys Lett. 2010; 494:326–330.
41. Nielsen AB, Straaso LA, Nieuwkoop AJ, Rienstra CM, Bjerring M, Nielsen NC. Broadband heteronuclear solid-state NMR experiments by exponentially modulated dipolar recoupling without decoupling. J Phys Chem Lett. 2010; 1:1952–1956. [PubMed: 20689682]
42. Lin J, Griffin RG, Khaneja N. Recoupling in solid state NMR using gamma prepared states and phase matching. J Magn Reson. 2011; 212:402–411. [PubMed: 21889380]
43. Li Y, Berthold DA, Frericks HL, Gennis RB, Rienstra CM. Partial C-13 and N-15 chemical-shift assignments of the disulfide-bond-forming enzyme DsbB by 3D magic-angle spinning NMR spectroscopy. ChemBioChem. 2007; 8:434–442. [PubMed: 17285659]
44. Artemov D, Bhujwalla ZM, Glickson JD. Band-selective heteronuclear cross polarization in liquids. J Magn Reson, Ser B. 1995; 107:286–288. [PubMed: 7788100]
45. Demers JP, Vijayan V, Becker S, Lange A. Tailored low-power cross-polarization under fast magic-angle spinning. J Magn Reson. 2010; 205:216–223. [PubMed: 20570194]
46. Neue G, Dybowski C. Determining temperature in a magic-angle spinning probe using the temperature dependence of the isotropic chemical shift of lead nitrate. Solid State Nucl Magn Reson. 1997; 7:333–336. [PubMed: 9176939]
47. Fung BM, Khitrin AK, Ermolaev K. An improved broadband decoupling sequence for liquid crystals and solids. J Magn Reson. 2000; 142:97–101. [PubMed: 10617439]
48. Morcombe CR, Zilm KW. Chemical shift referencing in MAS solid state NMR. J Magn Reson. 2003; 162:479–486. [PubMed: 12810033]
49. Harris RK, Becker ED, De Menezes SMC, Goodfellow R, Granger P. NMR nomenclature. Nuclear spin properties and conventions for chemical shifts – (IUPAC recommendations, 2001). Pure Appl Chem. 2001; 73:1795–1818.
50. Hediger S, Meier BH, Ernst RR. Adiabatic passage Hartmann–Hahn cross-polarization in NMR under magic-angle sample-spinning. Chem Phys Lett. 1995; 240:449–456.
51. Rienstra CM, Hohwy M, Hong M, Griffin RG. 2D and 3D N-15–C-13–C-13 NMR chemical shift correlation spectroscopy of solids: assignment of MAS spectra of peptides. J Am Chem Soc. 2000; 122:10979–10990.
52. Franks WT, Kloepper KD, Wylie BJ, Rienstra CM. Four-dimensional heteronuclear correlation experiments for chemical shift assignment of solid proteins. J Biomol NMR. 2007; 39:107–131. [PubMed: 17687624]
53. Franks WT, Zhou DH, Wylie BJ, Money BG, Graesser DT, Frericks HL, Sahota G, Rienstra CM. Magic-angle spinning solid-state NMR spectroscopy of the beta 1 immunoglobulin binding domain of protein G (GB1): N-15 and C-13 chemical shift assignments and conformational analysis. J Am Chem Soc. 2005; 127:12291–12305. [PubMed: 16131207]
54. Delaglio F, Grzesiek S, Vuister GW, Zhu G, Pfeifer J, Bax A. NMRPIPE: a multidimensional spectral processing system based on UNIX pipes. J Biomol NMR. 1995; 6:277–293. [PubMed: 8520220]
55. Goddard, TD.; Kneller, DG. Sparky 3. University of California; San Francisco:
56. Mehring, M. Principles of High Resolution NMR in Solids. 2. Springer-Verlag; New York: 1983.
57. Alemany LB, Grant DM, Alger TD, Pugmire RJ. Cross polarization and magic angle sample spinning NMR spectra of model organic compounds. 3. Effect of the 13C–1H dipolar interaction on cross polarization and carbon-proton dephasing. J Am Chem Soc. 1983; 105:6697–6704.

58. Fu R, Hu J, Cross TA. Towards quantitative measurements in solid-state CPMAS NMR: a Lee–Goldburg frequency modulated cross polarization scheme. J Magn Reson. 2004; 168:8–17. [PubMed: 15082244]

59. Veshtort M, Griffin RG. SPINEVOLUTION: a powerful tool for the simulation of solid and liquid state NMR experiments. J Magn Reson. 2006; 178:248–282. [PubMed: 16338152]

60. Herbst C, Herbst J, Leppert J, Ohlenschlaeger O, Gorlach M, Ramachandran R. Chemical shift correlation at high MAS frequencies employing low-power symmetry-based mixing schemes. J Biomol NMR. 2011; 50:277–284. [PubMed: 21674236]

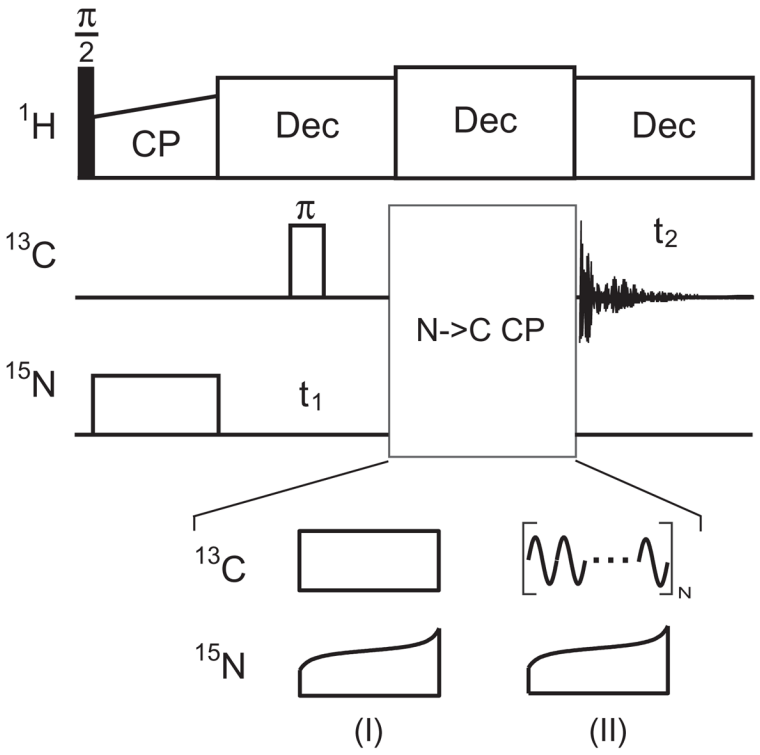

Fig. 1.

Pulse sequences used in 2D ^{15}N–^{13}C heteronuclear correlation experiments in solid-state MAS NMR. (I) The standard ^{15}N–^{13}C CP where the ^{15}N RF amplitude is tangent but the ^{13}C RF amplitude remains constant. (II) The sine modulated scheme where the ^{15}N RF amplitude is tangent while the ^{13}C RF amplitude is sinusoidally modulated at a given modulation frequency ω_m.

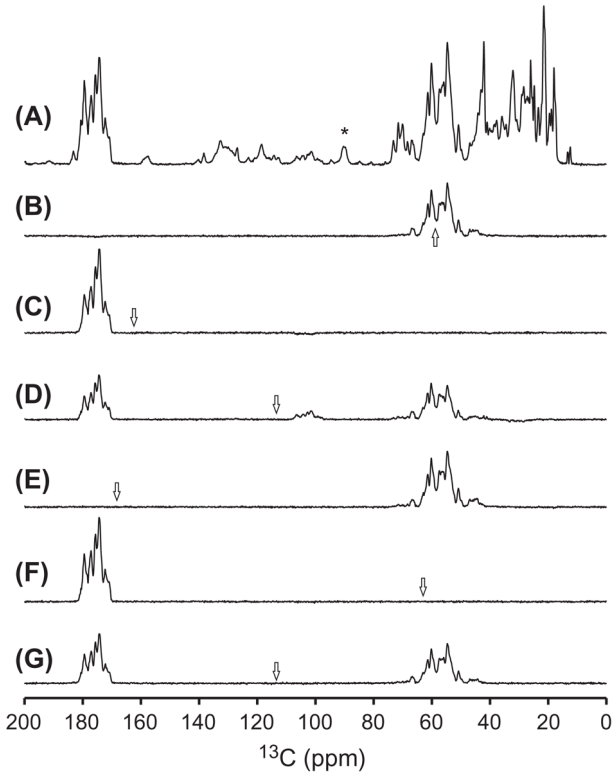

Fig. 2.

1D ^{13}C CP/MAS spectra of uniformly ^{13}C,^{15}N-labeled GB1 protein: (A) ^{13}C spectrum directly polarized from ^{1}H. The asterisk indicates the signal of a spacer used to provide a better sealing of the rotor. (B–G) Double cross polarized ^{13}C spectra using different N → C polarization conditions, normalized with the spectrum in (A) to illustrate their polarization efficiency. The arrows in the spectra indicate the $_{13}C$ carrier position in the experiments. The single-band selective SPECIFIC CP NCA (B) using ω_{1N} = 9.0 kHz with 10% tangent ramp and ω_{1C} = 3.0 kHz, and NCO (C) spectra using ω_{1N} = 7.0 kHz with 15% tangent ramp and ω_{1C} = 4.4 kHz. The dual-band rectangular DCP ^{13}C spectrum (D) using ω_{1N} = 7.0 kHz with 11% tangent ramp and ω_{1C} = 16.0 kHz. The NCA (E) and NCO (F) spectra using the sine modulated ^{13}C RF field with the amplitude of ω_{1C}^{max}=6.0 kHz and ω_m = 16.667 kHz and ω_{1N} = 9.0 kHz with 10% and 17% tangent ramp, respectively. The dual-band selective ^{13}C smDCP spectrum (G) using the sine modulated ^{13}C RF field with the amplitude of ω_{1C}^{max}=6.0 kHz and ω_m = 8.889 kHz and ω_{1N} = 9.0 kHz with 13% tangent ramp. The nominal RF amplitudes were calculated assuming a fine linearity of the Varian linear amplifier, which should have an accuracy of 0.5 kHz. In all experiments, 64 transients were used to accumulate the signals with a recycle delay of 3.5 s.

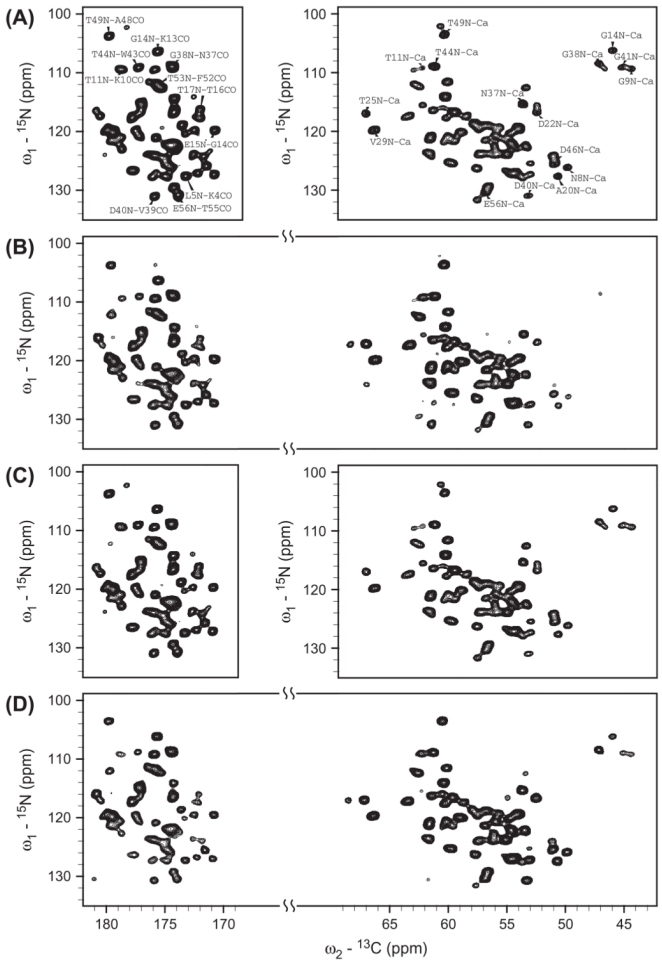

Fig. 3.

2D ^{15}N–^{13}C heteronuclear correlation spectra of uniformly ^{13}C,^{15}N-labeled GB1 protein using different N → C polarization conditions. (A) Single-band SPECIFIC ^{15}N–$^{13}C\alpha$ (Right) and ^{15}N–$^{13}C'$ (Left) spectra recorded in two separate experiments with the same experimental parameters as in Fig. 2B and C, respectively. (B) Dual-band rectangular DCP ^{15}N–$^{13}C\alpha/^{13}C'$ spectrum using the same parameters as in Fig. 2D. (C) Single-band selective ^{15}N–$^{13}C\alpha$ (Right) and ^{15}N–$^{13}C'$ (Left) smDCP spectra recorded in two separate experiments with the same experimental conditions as in Fig. 2E and F, respectively. (D) Dual-band selective ^{15}N–$^{13}C\alpha/^{13}C'$ smDCP spectrum using the same parameters as in Fig. 2G. The spectra were processed by nmrPipe [54] and plotted with Sparky [55]. In all experiments, 40 transients were used to accumulate the signals for each t_1 increment with a recycle delay of 3.5 s.

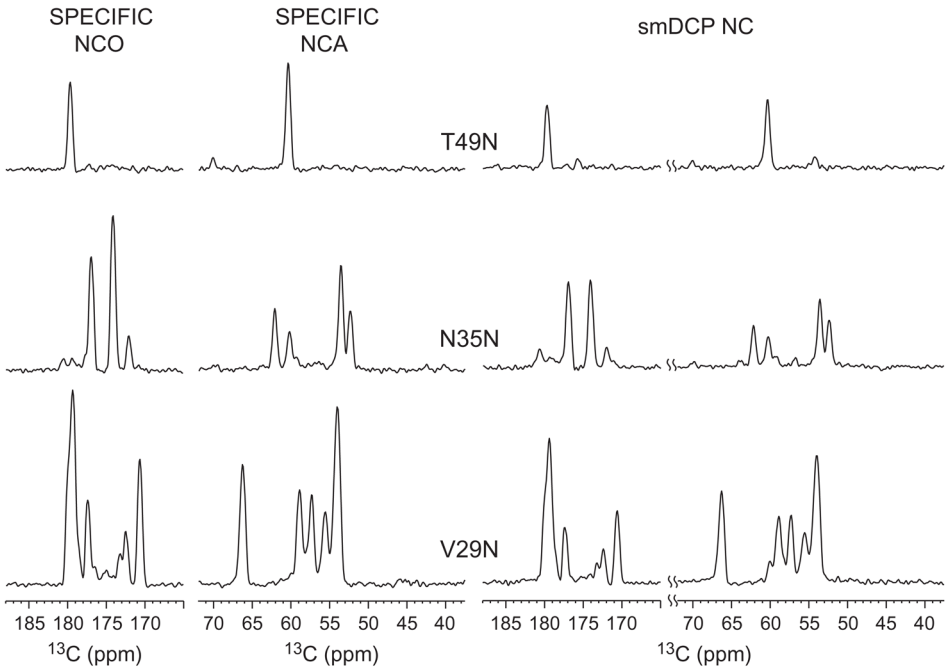

Fig. 4.

1D slices taken from the SPECIFIC NCO/NCA spectra in Fig. 3A and from the smDCP NC spectrum in Fig. 3D along T49 N (Top), N37N (Middle), and V29N (Bottom).

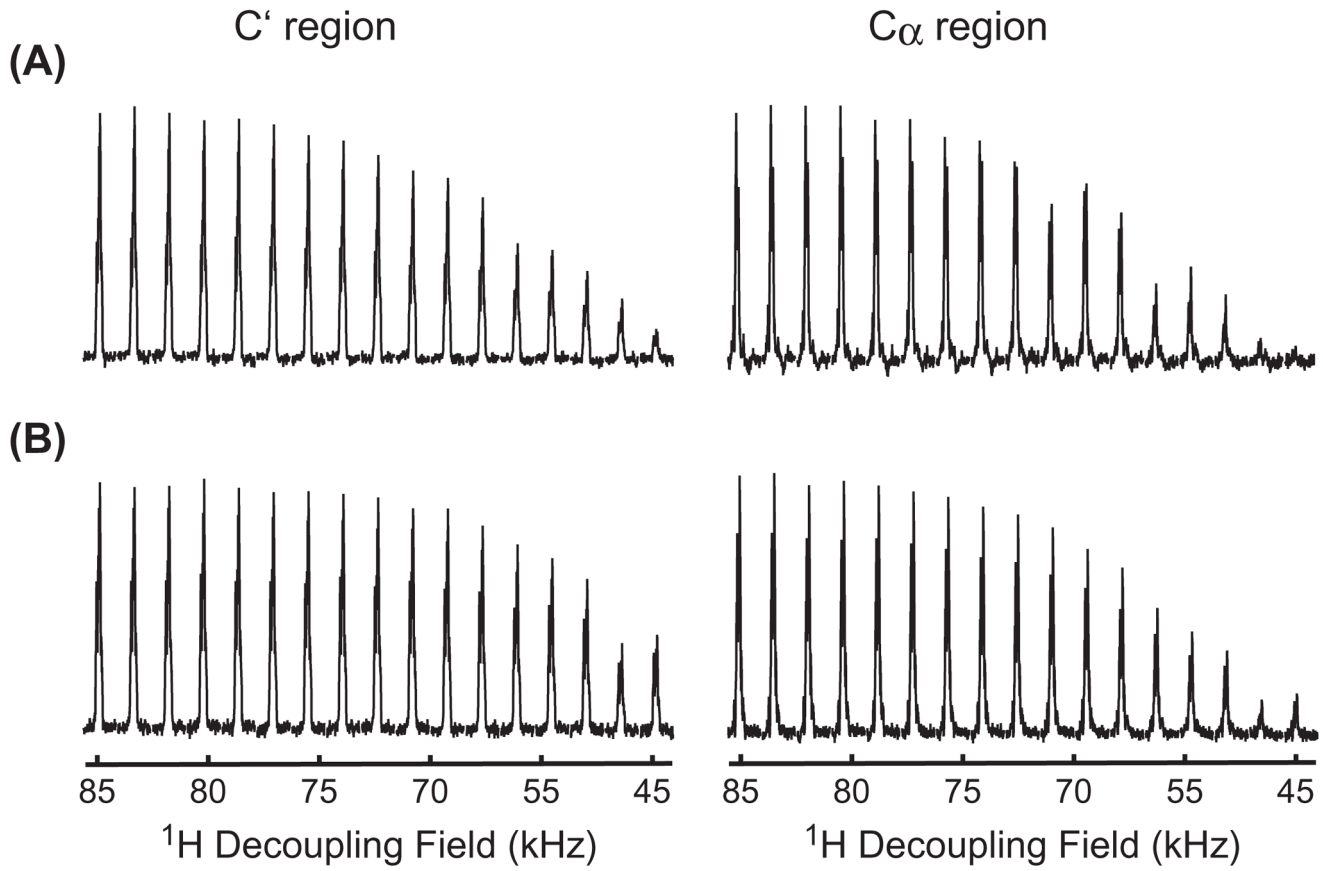

Fig. 5.

Dependence of the N → C polarization efficiency as a function of the ^{1}H decoupling amplitude during the N → C contact time in different N → C polarization schemes. (A) The dual-band rectangular DCP using the parameters in Fig. 2D. (B) The dual-band smDCP using the parameters in Fig. 2G.

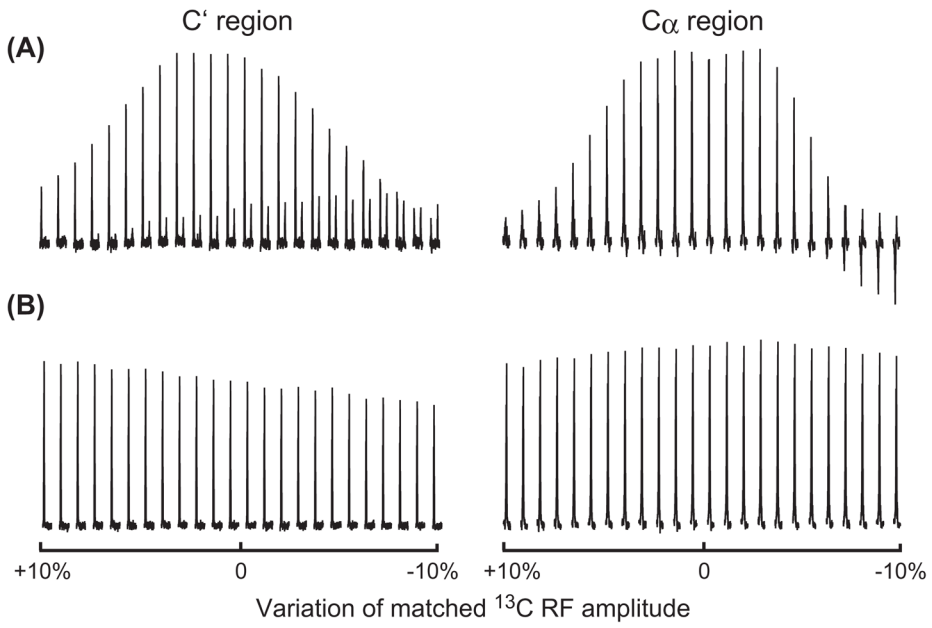

Fig. 6.

Instability effect of ^{13}C RF field on the N → C polarization efficiency in different schemes. The ^{13}C RF amplitude was varied by ±10% of the optimized values (set to 0) in Fig. 2D and G.

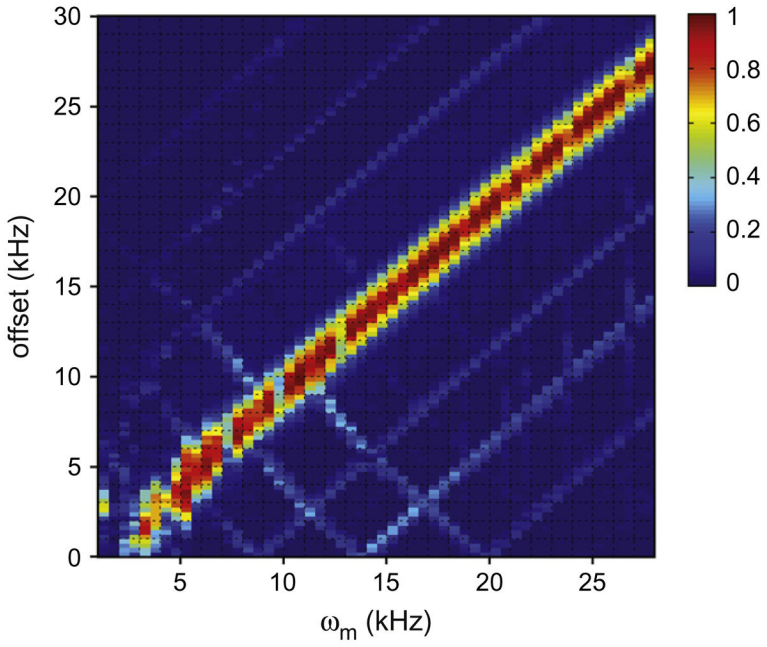

Fig. 7.

Simulated selectivity of the sine modulated scheme (e.g. Fig. 1II) as a function of offset and modulation frequency ω_m. The SPINEVOLUTION [59] was used for the simulations. For simplicity, a constant ^{15}N RF-field was utilized, and the spin system was ^{15}N–^{13}C, with a distance of r_{C-N} = 1.448 Å. The chemical shift parameters for ^{13}C were δ_{iso} = 0 ppm, δ_{aniso} = 24 ppm, η = 0.92; for ^{15}N, δ_{iso} = 0 ppm, δ_{aniso} = 100 ppm, η = 0.8. In the simulations, ω_{1N} = 9 kHz, ω_{1C}^{max}=6 kHz, and the MAS rate of 11 kHz were used. The maximum intensity in this plot was normalized to 1.